Self vAlidating Mueller matrix Micro – Mesoscope (SAMMM) for the characterization of biological media

Article *in* Optics Letters · March 2020

DOI: 10.1364/OL.387747

6 authors, including:

Ilyas Saytashev
Florida International University
25 PUBLICATIONS **93** CITATIONS

SEE PROFILE

Joseph Chue-Sang
National Institute of Standards and Technology
21 PUBLICATIONS **37** CITATIONS

SEE PROFILE

Jessica C Ramella-Roman
Florida International University
166 PUBLICATIONS **2,130** CITATIONS

SEE PROFILE

Self vAlidating Mueller matrix Micro - Mesoscope (SAMMM) for the characterization of biological media

ILYAS SAYTASHEV,[1,2] SUDIPTA SAHA,[2] JOSEPH CHUE-SANG,[2] PEDRO LOPEZ,[1] MEGAN LAUGHREY,[1] JESSICA C. RAMELLA-ROMAN[1,2*]

[1]*Department of Ophthalmology, Herbert Wertheim College of Medicine, Florida International University, 11200 SW 8th Street, Miami, FL 33199, USA*

[2]*Department of Biomedical Engineering, College of Engineering and Computing, Florida International University, 10555 West Flagler Street, Miami, FL 33174, USA*

**Corresponding author: jramella@fiu.edu*

Received XX Month XXXX; revised XX Month, XXXX; accepted XX Month XXXX; posted XX Month XXXX (Doc. ID XXXXX); published XX Month XXXX

Reflectance Mueller matrix polarimetry is being used to characterize biological media in multiple clinical applications. The origin of the reflectance polarimetric data is often unclear due to the impact of multiple scattering and tissue heterogeneity. We have developed a new multimodal imaging technique combining Mueller matrix reflectance, Mueller matrix digital confocal imaging and co-registered nonlinear microscopy techniques. The instrument unveils the origin of reflectance polarimetric signature in terms of confocal reflectance data. The reconstructed reflected Mueller matrix demonstrates the capability of our method to provide depth-resolved 3D polarization response from complex biological media in terms of depolarization, retardance and orientation parameters.

http://dx.doi.org/10.1364/OL.99.099999

Polarization-based imaging techniques are becoming of widespread use due to their unique ability to target structural components in both excised and live biological tissue. Mueller matrix polarimetry (MMP) has been used extensively in the determination of orientation and retardance of fibrous tissues due to its ability to measure birefringence [1, 2]. In parallel to preclinical and clinical work, multiple studies have been conducted to better understand how polarized light travels through and interacts with biological media[2]. In the past, polarized light transfer modeling has been approached through stochastic models and from a wave equation standpoint [3-6]. Currently, fundamental experimental work utilizing standards [7-10] has shown how different incident polarization states are maintained while travelling into a multi-scattering media. At the same time, different ways of decomposing the 4x4 Mueller matrix demonstrate the important need to simplify and access the basic medium polarimetry parameters, namely, diattenuation, retardance, and depolarization [7, 11, 12]. As physicians and scientists move these polarization modalities into complex biological environments, our understanding of the collected signal is limited by both the lack of well-characterized phantoms [13] mimicking such complexity and of mathematical models that take such complexity into account. The work described in this paper and the instrumentation at its core addresses in part this interesting unsolved problem. We have developed an instrument that combines two polarization imaging techniques, Mueller matrix reflectance and Mueller matrix confocal polarimetry [14], and integrated these modalities into a nonlinear microscope[15, 16]. A system that combines confocal Mueller matrix polarimetry and nonlinear microscopy has previously been proposed by Okoro et al. [17]. In their work the confocal Mueller matrix image was related to the co-registered nonlinear data and even used to pattern the Mueller matrix images for better analysis. Similarly, Bancelin et al. demonstrated through two independent imaging systems that second harmonic generation (SHG) microscopy and transmission Mueller matrix microscopy provide comparable information about arrangement of anisotropic structures [18]. Our intent here is different yet builds on these approaches - we have an added capability which allows for the collection of the back-reflected Mueller matrix (MM) image together with the depth-dependent confocal Mueller matrix and nonlinear images. The back-reflected MM images contain the signals reflected from the total volume (bulk) of the sample. Using our system we can study the origin of the back-reflected MM, which is most commonly used in clinical applications [13, 19, 20]. We can thus improve our understanding of the cumulative effect of photons traveling through multiply scattering media on the bulk reflected depolarization, retardance and diattenuation.

The combined nonlinear and MMP imaging setup is shown in Fig. 1. A pre-compensated beam from a broadband femtosecond laser (Element 600, Femtolasers, Vienna, Austria) is directed into a home-built laser scanning microscope, where it is focused into a specimen through a long working distance objective (Mitutoyo 5x/0.14NA). Reflected

light at fundamental wavelength range (700-900 nm) is separated from epi-detected two-photon excitation fluorescence (TPEF) and SHG by a short-pass dichroic mirror (650 nm, Chroma Technology Corp., Bellows Falls, VT) and directed to an output port by a 10:90 non-polarizing beam splitter placed between scanning and tube lenses of a microscope. The optical signal through the beam splitter is filtered with a bandpass filter (780 nm central wavelength, 10 nm FWHM) and collected by a CMOS camera (PCO-Edge 5.5, PCO AG, Kelheim, Germany) which is placed at the conjugate imaging plane. The CMOS sensor active area is 5.7x4.28 mm^2 with a physical pixel size of 2.2 µm. A 7x7 binning is applied to a camera increasing the framerate to 120 fps and reducing the resolution to 368x276 $pixels^2$ with an effective pixel size of 15.4 µm. The nonlinear SHG and TPEF optical signals are separated using second dichroic mirror (440 nm, Chroma Technology Corp., Bellows Falls, VT) and detected by respective photosensor (H10720-210, Hamamatsu Photonics K.K., Shizuoka, Japan) with suitable bandpass filters (Semrock 400 nm/30 nm and 500 nm/24 nm, IDEX Health & Science LLC, Rochester, NY).

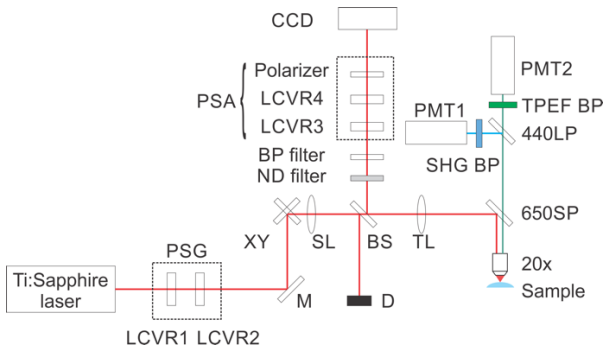

Figure 1: Schematic diagram of co-registered nonlinear and MMP laser scanning microscope.

Mueller matrix polarimetry imaging is enabled by an addition of a polarization state generator (PSG) at the microscope input, and a polarization state analyzer (PSA) before the camera in the linear reflectance arm. Both PSA and PSG consist of a pair of liquid crystal variable retarders (LCVRs, Meadowlark Optics, Frederick, CO) and a linear polarizer (LPNIR100, Thorlabs Inc., Newton, NJ) oriented parallel to the reference plane (optical bench). We omit the linear polarizer in the PSG since the laser itself is polarized parallel to the reference plane. All four LCVRs are operated by a D3040 USB controller (Meadowlark Optics, Frederick, CO). The laser beam is scanned across the sample with a pair of galvanometer mirrors (GVS102, Thorlabs Inc., Newton, NJ). For each scanning position, the back-propagated nonlinear signal is collected by a pair of photo multiplier tube (PMT) detectors and a DAQ board (PCIe-6351, National Instruments, Austin, TX) simultaneously.

During acquisition the camera records one frame for each laser position containing a reflection from the imaged sample. To remove out-of-focus signal, our software defines active pixels on a camera according to pre-calibrated laser beam scanning position and the virtual pinhole size d [21]; the adjustable confocal parameter d is set to 5 pixels leading to approx. 10 µm axial resolution. Pixel intensities inside the defined mask of each acquired frame are ultimately added to the output image. Intensity image for back-reflected MM is created by adding all acquired camera frames without applying virtual pinhole. After laser scans through the sample by a predetermined pattern (trigonal scan 128x128 $pixels^2$), four output images are reconstructed: TPEF, SHG, confocal reflectance and back-reflected MM for each PSG and PSA states. The resulting output on each imaging plane is a set of microscopic images: two are obtained from nonlinear channels and 24 are confocal intensity images from a camera. The pre-processing routine only applies an averaging filter with size of 2 pixels for the input images to reduce the noise.

The calibration of the MMP system is done using an external calibrated polarimeter (Thorlabs Inc., Newton, NJ). An optical filter (780 nm,10 nm FWHM) is temporarily placed in the beam path before LCVRs of PSG to restrict the laser bandwidth during calibration, and then removed once the calibration procedure is finished. The generated polarization states at the focal plane of the objective are: $[1\ 0.43\ 0.66\ 0.61]^T$, $[1\ -0.97\ 0.15\ 0.21]^T$, $[1\ -0.52\ -0.75\ -0.40]^T$, $[1\ 0.50\ -0.14\ 0.85]^T$, $[1\ 0.28\ 0.87\ 0.40]^T$, $[1\ 0.80\ 0.09\ -0.60]^T$ with the largest RMS error of 0.4%. Similarly, the measured four output Stokes vectors are, $[1\ 0.33\ 0.76\ -0.49]^T$, $[1\ 0.23\ -0.58\ 0.77]^T$, $[1\ -0.88\ 0.52\ 0.40]^T$, $[1\ 0.26\ -0.76\ 0.68]^T$ with 3% RMS error. Using these states, a reflectance intensities matrix is obtained and after few algebraic manipulation the Mueller matrix can be constructed [2, 14]. Once LCVRs of PSG and PSA are set to the calibrated values, the system's MM M_{sys} is measured using a mirror and placed at the focal plane of an objective.

The decomposition of the sample's Mueller matrix M_s as proposed by Lu-Chipman [11], yields three canonical matrices accounting for material depolarization M_Δ; retardance, optical activity M_R, and diattenuation M_D: $\boldsymbol{M_s = M_\Delta M_R M_D}$. Further, linear retardance and orientation of fast optical axis can be calculated from a retardance matrix M_R. Mueller matrix retrieval and decomposition at each pixel results in images of depolarization, orientation and linear retardance maps. MM calculation, decomposition, and visualization are performed using MATLAB. Depth-resolved data is reconstructed as planes in 3D volume for all calculated polarization parameters as well as nonlinear images to demonstrate the dynamic change with depth. Hence our Self vAlidating Mueller matrix Micro - Mesoscope (SAMMM) can be used to confirm if the changes in the Mueller matrix of the depth dependent data are due to a birefringence or other types of interaction. To demonstrate the system capability, we imaged two types of model samples: (i) an optical phantom made of titanium dioxide showing only depolarization effect and (ii) a nylon fiber placed in a highly scattering medium (milk) having both depolarization and retardance effects.

The optical phantom consisting of titanium dioxide was used for recording both the confocal and back-reflected MM images. In Fig. 2(a), we show the variation of average polarization-independent reflectance intensity (given by M_{11}) with depth from the surface of the phantom from a region of

the optical phantom. The corresponding depolarization coefficients are shown in Fig 2(b). The variation of these parameters with different confocal pinhole sizes are shown by 1x1, 3x3, 5x5 and 7x7. Here 1x1, 3x3, 5x5 and 7x7 represent pinholes with effective radius of 16 μm, 48 μm, 80 μm and 112 μm, respectively. As expected with increasing depth, depolarization increases. Increasing pinhole size yields higher M_{11} values however, the depolarization does not vary significantly. For back reflectance the recorded M_{11} and the corresponding depolarization remains the same for all depths. It is important to note that the depolarization in back reflectance MM is higher than the depolarization in confocal MM measurements, but the values asymptotically converge. We utilize a previously developed Monte Carlo model of polarized light transfer to model the interaction of titanium dioxide phantom with polarized light both for back-reflected MM and confocal Mueller Matrix imaging. A confocal pinhole is added to the program following the approach by Tanbakuchi et al. [22]. Model parameters are $\mu_a = 0.33\ cm^{-1}$, $\mu_s = 62.5\ cm^{-1}$ average particle radius = 0.135 μm, n = 2.5 for the particle and 1.54 medium, following the report of Firbank et al. [23] with the laser wavelength of 0.78 μm. 10 million photons are used in the simulation. Fig. 2(b) shows a good agreement of Monte-Carlo simulation results (black symbols) with the experimental findings (colored symbols).

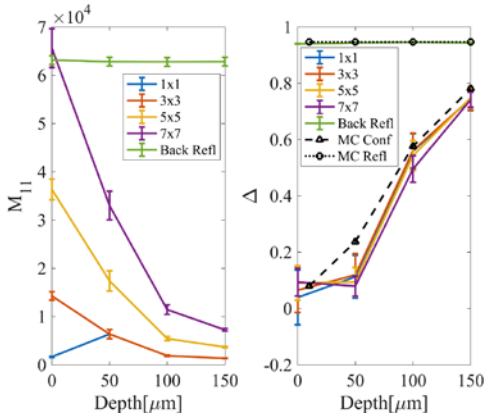

Figure 2: (a) Polarization independent unnormalized (average) intensity M_{11} from a region of titanium dioxide phantom and (b) depolarization coefficient for different pinhole size in confocal Mueller matrix and back reflected Mueller matrix geometry as a function of distance from the surface of the phantom for one region of interest. The Monte Carlo simulated depolarization coefficients for both the confocal (MC Conf) and back-reflected MM (MC Refl) are also shown by black dashed and dotted lines, respectively.

In second experiment we imaged a nylon fiber submerged in a milk solution. The choice of nylon fiber is motivated by the fact that it is known to possess high birefringence properties while the milk is highly scattering and has been used to mimic biological media. The idea is to show how our method can capture/differentiate the actual polarization properties arising from the local environmental anisotropies. A total of 41 planes were imaged with a step size of 10 μm starting from the surface of the sample. In Fig. 3, we have shown the SHG, M_{11}, depolarization and linear retardance at different depths from this sample. At the beginning, the imaging plane does not include the fiber, we only observe the signal from the milk solution, however after about 80 μm from the surface we start seeing the images of the fiber in both SHG (column 1) and M_{11} (column 2) images. The corresponding depolarization and linear retardance are shown in column 3 and 4, respectively.

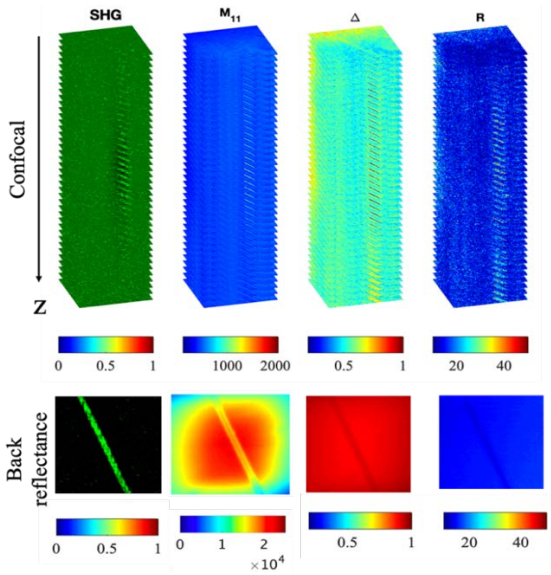

Figure 3: Top panel: Depth-resolved SHG, confocal M_{11}, depolarization and linear retardance (degrees) images of nylon fiber placed in milk solution; bottom panel: the corresponding quantities in back reflectance. SHG signal is square-rooted for visualization purpose. Size of the imaging area is 240x240 μm^2.

When the imaging plane meets the fiber, we notice that the depolarization and linear retardance of the fiber are higher than the surrounding milk. After the imaging plane crosses the fiber and we no longer see the image of the fiber in SHG and M_{11} images while the corresponding depolarization and retardance images maintain a memory of the interaction as expected. This is true for all subsequent layers, although interaction with the milk does distort the subsequent images. The bottom row shows the back reflectance SHG, M_{11}, depolarization and linear retardance, respectively, from the entire sample.

Numerical analysis of the data for all layers shows that the effect of the polarized light on the birefringent nylon fiber is position dependent (Fig. 4). To illustrate this, depolarization from two regions of interest – at the central portion and on the side of a nylon fiber – is plotted against the imaging depth. The imaging layer containing the nylon fiber can be clearly visualized through the SHG data (dotted black line); the confocal depolarization observed at the center of the fiber decreases as we approach the imaging layer with a nylon fiber possibly due to a heightened specular reflectance while the opposite is true when we analyze depolarization on the side region of the fiber. In back reflectance the depolarization does not change significantly as the objective moves closer to the sample but the results on the depolarization are still position dependent.

Values selected from the center of the fiber have higher retardance and lower depolarization than the values collected on the side, (a student T test conducted on the data on the center of the fiber and on the side shows a p value of 0.02 on average).

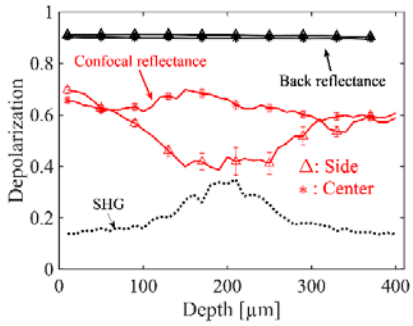

Figure 4: Depolarization in confocal (red) and back reflectance (black). SHG signal (black dotted line) demonstrates the presence of a nylon fiber in the middle of a depth scan. Legends 'Side' (Δ) and 'Center' (*) refer to the region at the central and side portions of the nylon fiber in both confocal and back reflectance data.

Finally, we show an application of our system to biological media. A rat cornea was stained with DAPI (Fig. 5) marking the presence of epithelial cells and keratocytes. Tightly packed epithelial layer cells slowly depolarize light, this effect increases as the image plane crosses the stromal anterior layer and exhibits higher values reaching the posterior stroma. The presence of both TPEF and SHG signal in 0 μm imaging layer suggests that imaging plane was at the Bowman's layer (superficial layer between epithelium and the stroma in the cornea), therefore containing signals from epithelium cells (TPEF) and stromal collagen (SHG). A clear separation among epithelium and stromal layers is noticeable in the linear retardation and orientation volumes.

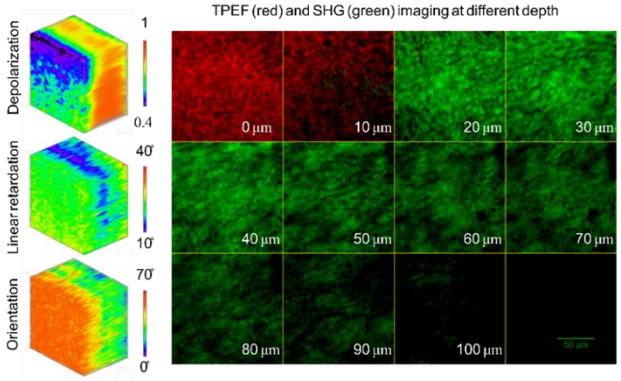

Figure 5. Full-depth two-photon and confocal MMP imaging of an unstained rat cornea. 120x120 μm² imaging area was taken at the center of a cornea.

In conclusion, our SAMMM system can provide depth-resolved confocal and back reflectance Mueller matrix imagery as well as co-registered SHG and TPEF for validation. We have begun exploring how polarized light travels through a scattering media and depolarizes, we have also shown that the depolarization and retardance caused by a birefringent fiber is influenced by its shape and location. The initial results on an excised rat cornea demonstrate clear depth resolved regions of polarization sensitive interaction. All this bring into question current decomposition methods particularly for back reflectance MM images, these methods cannot account for discrete transitions such as the ones shown in Fig. 3 and Fig. 5. Our future work will focus on this issue evaluating the error associated with the decomposition methods in layered biological media.

Acknowledgement: Jefferson Gomes for cornea sample preparation.
Support: Herbert and Nicole Wertheim Professorship Endowment (All authors) NSF.DMR 1548924 (JRR, SS) NSF.EEC-1648451(JRR, IS, JC).
Disclosures: The authors declare no conflicts of interest.

References

1. V. V. Tuchin, J Biomed Opt **21** (2016).
2. N. Ghosh, and I. A. Vitkin, J Biomed Opt **16** (2011).
3. M. R. Antonelli, A. Pierangelo, T. Novikova, P. Validire, A. Benali, B. Gayet, and A. De Martino, Opt Express **18**, 10200-10208 (2010).
4. P. Ghassemi, L. T. Moffatt, J. W. Shupp, and J. C. Ramella-Roman, Journal of Biophotonics **9**, 100-108 (2016).
5. J. Ramella-Roman, S. Prahl, and S. Jacques, Opt. Express **13**, 4420-4438 (2005).
6. T. Yun, N. Zeng, W. Li, D. Li, X. Jiang, and H. Ma, Opt. Express **17**, 16590-16602 (2009).
7. M. Sun, H. He, N. Zeng, E. Du, Y. Guo, S. Liu, J. Wu, Y. He, and H. Ma, Biomedical Optics Express **5**, 4223-4234 (2014).
8. T. S. Eliasdottir, D. Bragason, S. H. Hardarson, G. Kristjansdottir, and E. Stefansson, Graefe's archive for clinical and experimental ophthalmology = Albrecht von Graefes Archiv fur klinische und experimentelle Ophthalmologie (2015).
9. S. Rehn, A. Planat-Chretien, M. Berger, J. M. Dinten, C. Deumie, and A. da Silva, J Biomed Opt **18**, 16007 (2013).
10. A. Da Silva, C. Deumié, and I. Vanzetta, Biomedical Optics Express **3**, 2907-2915 (2012).
11. S. Y. Lu, and R. A. Chipman, Journal of the Optical Society of America a-Optics Image Science and Vision **13**, 1106-1113 (1996).
12. R. Ossikovski, A. De Martino, and S. Guyot, Opt Lett **32**, 689-691 (2007).
13. J. Chue-Sang, M. Gonzalez, A. Pierre, M. Laughrey, I. Saytashev, T. Novikova, and J. C. Ramella-Roman, J Biomed Opt **24**, 1-12, 12 (2019).
14. D. Lara, and C. Dainty, Optics Letters **30**, 2879-2881 (2005).
15. J. M. Bueno, F. J. Ávila, and P. Artal, Microscopy and Analysis (2016).
16. W. Denk, J. H. Strickler, and W. W. Webb, Science **248**, 73-76 (1990).
17. C. Okoro, and K. C. Toussaint, J Biomed Opt **22** (2017).
18. S. Bancelin, A. Nazac, B. H. Ibrahim, P. Dokladal, E. Decenciere, B. Teig, H. Haddad, H. Fernandez, M. C. Schanne-Klein, and A. De Martino, Opt. Express **22**, 22561-22574 (2014).
19. S. Alali, and A. Vitkin, J Biomed Opt **20** (2015).
20. J. Chue-Sang, N. Holness, M. Gonzalez, J. Greaves, I. Saytashev, S. Stoff, A. Gandjbakhche, V. V. Chernomordik, G. Burkett, and J. C. Ramella-Roman, J Biomed Opt **23** (2018).
21. E. Sanchez-Ortiga, G. Saavedra, M. Martinez-Corral, A. Doblas, and A. Calatayud, Eur-Am Worksh Info (2011).
22. A. A. Tanbakuchi, J. A. Udovich, A. R. Rouse, K. D. Hatch, and A. F. Gmitro, Am J Obstet Gynecol **202**, 90 e91-99 (2010).
23. M. Firbank, M. Oda, and D. T. Delpy, Phys Med Biol **40**, 955-961 (1995).

Full references:

1. Tuchin VV. Polarized light interaction with tissues. J Biomed Opt. 2016;21(7).
2. Ghosh N, Vitkin IA. Tissue polarimetry: concepts, challenges, applications, and outlook. J Biomed Opt. 2011;16(11).
3. Antonelli MR, Pierangelo A, Novikova T, Validire P, Benali A, Gayet B, et al. Mueller matrix imaging of human colon tissue for cancer diagnostics: how Monte Carlo modeling can help in the interpretation of experimental data. Opt Express. 2010;18(10):10200-8.
4. Ghassemi P, Moffatt LT, Shupp JW, Ramella-Roman JC. A new approach for optical assessment of directional anisotropy in turbid media. Journal of Biophotonics. 2016;9(1-2):100-8.
5. Ramella-Roman J, Prahl S, Jacques S. Three Monte Carlo programs of polarized light transport into scattering media: part I. Opt Express. 2005;13(12):4420-38.
6. Yun T, Zeng N, Li W, Li D, Jiang X, Ma H. Monte Carlo simulation of polarized photon scattering in anisotropic media. Opt Express. 2009;17(19):16590-602.
7. Sun M, He H, Zeng N, Du E, Guo Y, Liu S, et al. Characterizing the microstructures of biological tissues using Mueller matrix and transformed polarization parameters. Biomedical Optics Express. 2014;5(12):4223-34.
8. Eliasdottir TS, Bragason D, Hardarson SH, Kristjansdottir G, Stefansson E. Venous oxygen saturation is reduced and variable in central retinal vein occlusion. Graefe's archive for clinical and experimental ophthalmology = Albrecht von Graefes Archiv fur klinische und experimentelle Ophthalmologie. 2015.
9. Rehn S, Planat-Chretien A, Berger M, Dinten JM, Deumie C, da Silva A. Depth probing of diffuse tissues controlled with elliptically polarized light. J Biomed Opt. 2013;18(1):16007.
10. Da Silva A, Deumié C, Vanzetta I. Elliptically polarized light for depth resolved optical imaging. Biomedical Optics Express. 2012;3(11):2907-
11. Lu SY, Chipman RA. Interpretation of Mueller matrices based on polar decomposition. Journal of the Optical Society of America a-Optics Image Science and Vision. 1996;13(5):1106-13.
12. Ossikovski R, De Martino A, Guyot S. Forward and reverse product decompositions of depolarizing Mueller matrices. Opt Lett. 2007;32(6):689-91.
13. Chue-Sang J, Gonzalez M, Pierre A, Laughrey M, Saytashev I, Novikova T, et al. Optical phantoms for biomedical polarimetry: a review. J Biomed Opt. 2019;24(3):1-12, .
14. Lara D, Dainty C. Double-pass axially resolved confocal Mueller matrix imaging polarimetry. Optics Letters. 2005;30(21):2879-81.
15. Bueno JM, Ávila FJ, Artal P. Second harmonic generation microscopy: a tool for quantitative analysis of tissues. Microscopy and Analysis. 2016.
16. Denk W, Strickler JH, Webb WW. 2-Photon Laser Scanning Fluorescence Microscopy. Science. 1990;248(4951):73-6.
17. Okoro C, Toussaint KC. Second-harmonic patterned polarization-analyzed reflection confocal microscope. J Biomed Opt. 2017;22(8).
18. Bancelin S, Nazac A, Ibrahim BH, Dokladal P, Decenciere E, Teig B, et al. Determination of collagen fiber orientation in histological slides using Mueller microscopy and validation by second harmonic generation imaging. Opt Express. 2014;22(19):22561-74.
19. Alali S, Vitkin A. Polarized light imaging in biomedicine: emerging Mueller matrix methodologies for bulk tissue assessment. J Biomed Opt. 2015;20(6).
20. Chue-Sang J, Holness N, Gonzalez M, Greaves J, Saytashev I, Stoff S, et al. Use of Mueller matrix colposcopy in the characterization of cervical collagen anisotropy. J Biomed Opt. 2018;23(12).
21. Sanchez-Ortiga E, Saavedra G, Martinez-Corral M, Doblas A, Calatayud A. Confocal scanning microscope using a CCD camera as a pinhole-detector system. Eur-Am Worksh Info. 2011.
22. Tanbakuchi AA, Udovich JA, Rouse AR, Hatch KD, Gmitro AF. In vivo imaging of ovarian tissue using a novel confocal microlaparoscope. Am J Obstet Gynecol. 2010;202(1):90 e1-9.
23. Firbank M, Oda M, Delpy DT. An improved design for a stable and reproducible phantom material for use in near-infrared spectroscopy and imaging. Phys Med Biol. 1995;40(5):955-61.